Forecast Applications of GLM Gridded Products: A Data Fusion Perspective

KEVIN C. THIEL[a,b,c,d] KRISTIN M. CALHOUN,[c] AND ANTHONY E. REINHART[c]

[a] Cooperative Institute for Severe and High-Impact Weather Research and Operations, University of Oklahoma, Norman, Oklahoma
[b] NWS Storm Prediction Center, Norman, Oklahoma
[c] NOAA/OAR National Severe Storms Laboratory, Norman, Oklahoma
[d] School of Meteorology, University of Oklahoma, Norman, Oklahoma

ABSTRACT: The recently deployed GOES-R series Geostationary Lightning Mapper (GLM) provides forecasters with a new, rapidly updating lightning data source to diagnose, forecast, and monitor atmospheric convection. Gridded GLM products have been developed to improve operational forecast applications, with variables including flash extent density (FED), minimum flash area (MFA), and total optical energy (TOE). While these gridded products have been evaluated, there is a continual need to integrate these products with other datasets available to forecasters such as radar, satellite imagery, and ground-based lightning networks. Data from the Advanced Baseline Imager (ABI), Multi-Radar Multi-Sensor (MRMS) system, and one ground-based lightning network were compared against gridded GLM imagery from GOES-East and GOES-West in case studies of two supercell thunderstorms, along with a bulk study from 13 April to 31 May 2019, to provide further validation and applications of gridded GLM products from a data fusion perspective. Increasing FED and decreasing MFA corresponded with increasing thunderstorm intensity from the perspective of ABI infrared imagery and MRMS vertically integrated reflectivity products, and was apparent for more robust and severe convection. Flash areas were also observed to maximize between clean-IR brightness temperatures of 210–230 K and isothermal reflectivity at −10°C of 20–30 dBZ. TOE observations from both GLMs provided additional context of local GLM flash rates in each case study, due to their differing perspectives of convective updrafts.

SIGNIFICANCE STATEMENT: The Geostationary Lightning Mapper (GLM) is a lightning sensor on the current generation of U.S. weather satellites. This research shows how data from the space-based lightning sensor can be combined with radar, satellite imagery, and ground-based lightning networks to improve how forecasters monitor thunderstorms and issue warnings for severe weather. The rate of GLM flashes detected and the area they cover correspond well with radar and satellite signatures, especially in cases of intense and severe thunderstorms. When the GLM observes the same thunderstorm from the GOES-East and GOES-West satellites, the optical energy (brightness) of the flashes may help forecasters interpret the types of flashes observed from each sensor.

1. Introduction

Lightning data can provide a wealth of information for the operational and severe storms research communities related to thunderstorm microphysics, convective morphology, severity potential, and the hazard of lightning itself to the public. The formation of oppositely charged regions within convective clouds—which creates the necessary conditions for lightning flashes to initiate—is driven by the ambient thermodynamic, kinematic, and microphysical properties imparted on hydrometeors. Charge separation of hydrometeors within convective clouds frequently occurs in the mixed-phase region between the −10° and −40°C isotherms, as collisions between ice and graupel particles in the presence of supercooled liquid water impart opposing charges on the hydrometeors (Takahashi 1978; Emersic and Saunders 2010). Lightning flashes initiate between oppositely charged regions (MacGorman et al. 1981; Williams 1985), and the organization of the electrical potential controls the frequency and propagation of the flash (Bruning and MacGorman 2013). The presence of mixed-phase hydrometeors for thunderstorm electrification can be inferred from radar reflectivity at various altitudes (Hondl and Eilts 1994; Wolf 2006; Mosier et al. 2011) or dual-polarization radar variables (Woodard et al. 2012; Stolzenburg et al. 2015). Additionally, hydrometeor glaciation driven by convective updrafts creates cooling cloud tops which are observed from visible, near-infrared, and infrared satellite imagery (Roberts and Rutledge 2003; Elsenheimer and Gravelle 2019).

As a thunderstorm intensifies, lightning information provides insight into key processes related to its increasing severity potential. Growth of the updraft volume and increasing graupel mass coincide with rapid increases in lightning production, which can be a useful signal of impending hazards such as large hail, damaging winds, and tornadoes (Williams et al. 1999; Schultz et al. 2009, 2017). Additionally, trends in local flash rates are inversely related to the areal extent of lightning flashes (Bruning and MacGorman 2013; Calhoun et al. 2014), and an increasing frequency of spatially smaller flashes can also signal the growing severity potential of a thunderstorm (Schultz et al. 2015; Thiel et al. 2020). Features from radar and satellite imagery can also be used to identify

Corresponding author: Kevin Thiel, kevin.thiel@ou.edu

intensifying thunderstorms. Intense convective updrafts are frequently depicted from satellite imagery as decreasing local minima in infrared brightness temperatures (Roberts and Rutledge 2003), increasing isothermal areas of anvil shields (Makowski et al. 2013), overshooting tops (Adler et al. 1983; Bedka et al. 2010), and above anvil cirrus plumes (Bedka et al. 2018). The lofting of larger hydrometeors above the freezing level by the updraft can also be observed from increasing radar reflectivity at key isothermal levels and used to identify hail formation and precipitation loading as precursors to severe weather occurrence. Also, vertically integrated reflectivity products provide insight into the strength and severity potential of convective updrafts, along with their potential to produce lightning (Greene and Clark 1972; Witt et al. 1998; Carey and Rutledge 2000), and can be generated in three-dimensional rapidly updating reflectivity fields for operational and severe storms research applications (Smith et al. 2016).

Remotely sensed observations of lightning from ground-based networks have been leveraged by the forecasting and severe storms research communities (Rison et al. 1999; Cummins and Murphy 2009). Launch of the first Geostationary Operational Environmental Satellite (GOES)-R series Geostationary Lightning Mapper (GLM) (Goodman et al. 2013) in 2016 provided a new perspective of total lightning observations across the continental United States (CONUS) from GOES-East and GOES-West at 75° and 137°W, respectively. The GLM was designed with an average flash detection efficiency (DE) over the entire field of view of 70% and a false alarm rate of 5%. Several data validation efforts have attempted to describe and quantify the relative quality of GLM data over the CONUS region (Murphy and Said 2020; Zhang and Cummins 2020; Bateman et al. 2021), along with providing caveats when applying these data (Calhoun et al. 2018; Rutledge et al. 2020; Peterson 2021). Overall, the GLM exceeds the required 70% average DE during both the day and night (Bateman et al. 2021), with lower detection efficiencies within 2000 km of the edge of the field of view (Murphy and Said 2020). Gridded GLM imagery has been developed for research and operational applications to exploit information from of the spatial footprint of each lightning flash observed from the GLM (Bruning 2019; Bruning et al. 2019). These products were evaluated in NOAA's Hazardous Weather Testbed from 2018 to 2022 and provided insights into the operational value of products related to flash density, area, and optical energy (Calhoun 2019; Thiel and Calhoun 2021; Thiel 2022).

With two GLMs in geostationary orbit, there is a large region of sensor overlap from approximately 80° to 130°W. This provides the opportunity for GLM-to-GLM comparisons of the same thunderstorms. When comparing GLM data in these overlap regions, Rudlosky and Virts (2021) found spatial trends in relative DE and flash characteristics between the *GOES-16* and *GOES-17* GLMs. The *GOES-16* GLM (hereinafter GLM16) observes more flashes that are on average larger and less luminous when compared to the *GOES-17* GLM (hereinafter GLM17) east of 103°W, and vice versa west of 103°W. Further comparisons between the GOES-East and GOES-West GLMs may provide additional insights into

the variations of GLM data characteristics, their quality, and their operational forecast applications, especially when combined with other remote sensing observations. This study examines convection from the perspective of the GOES-East and GOES-West GLMs, with respect to merged reflectivity and satellite imagery datasets, in an attempt to identify key applications and caveats when using these datasets for severe thunderstorm identification and monitoring. Intercomparisons between datasets were examined through two case studies of discrete supercells in Kansas (24 May 2019) and Alabama (25 March 2021), along with a bulk 7-week study over the central and eastern United States in April and May of 2019.

2. Data and methods

a. Satellite data

The GOES-R series Geostationary Lightning Mappers (Goodman et al. 2012, 2013) provide continuous lightning observations over most of the Western Hemisphere between the ±54° latitudes (Rudlosky et al. 2019). Gridded GLM data from *GOES-16* and *GOES-17*, the operational instruments during the period of study, were generated using glmtools (Bruning 2019; Bruning et al. 2019) and include flash extent density (FED), minimum flash area (MFA), and total optical energy (TOE). Increasing FED and decreasing MFA values have been identified in thunderstorms with increasing updraft strength and severity potential (Thiel et al. 2020), similar to the relationships identified in recent numerical and observational studies (Calhoun et al. 2013, 2014; Schultz et al. 2015). Gridded data were accumulated over a 5-min interval, updated every minute, based upon consistent recommendations from the Hazardous Weather Testbed (HWT) to quickly diagnose convective trends (Calhoun 2018, 2019).

Infrared brightness temperatures from cloud top were collected from the Advanced Baseline Imager (Schmit et al. 2017), a 16-band radiometer on *GOES-16* and *GOES-17* (hereinafter ABI16 and ABI17). Radiance measurements across the CONUS scene, which updates every 5 min in Mode 6 (Super Flex), were used for the bulk study, and from the mesoscale and full disk scenes from ABI16 and ABI17, respectively, for the two case studies. Cloud-top infrared data are used in operational and scientific applications to interrogate convection initiation, updraft strength, and the potential to produce severe weather (Reynolds 1980; Roberts and Rutledge 2003; Thiel et al. 2020), along with GLM data quality (Peterson 2021). Imagery from the ABI16 10.3-μm "Clean-IR" band (Schmit et al. 2012) were used to manually identify overshooting tops in the supercell case studies using signatures consistent with Adler et al. (1985) and Bedka et al. (2010), along with using the approximate tropopause level from adjacent rawinsonde observations. In the bulk study, IR data from ABI16 were collected at cloud top by administering the ABI clear-sky mask (ACM) (Heidinger and Straka 2013) product on the IR data to remove the pixels classified as clear sky. Last, data from the ABI cloud-top height algorithm (Heidinger 2013) were collected in the bulk study to improve data quality as described later.

b. Ground-based data

Select products from the Multi-Radar Multi-Sensor (MRMS) System (Smith et al. 2016) were recorded for their ability to infer thunderstorm morphology, electrification processes, and variations in optical depth through layered and vertically integrated reflectivity and velocity products. MRMS provides reflectivity data from the Weather Surveillance Radar-1988 Doppler (WSR-88D) network on a 0.01° horizontal grid with 33 vertical levels, and new data are made available operationally every 2 min. Isothermal reflectivity at −10°C and vertically integrated ice (VII) (Mosier et al. 2011; Carey and Rutledge 2000) were selected for their ability to represent the amount of graupel within the convective updraft and therefore provide context to a thunderstorm's total lightning production (Schultz et al. 2015; Carey et al. 2019). Additionally, changes in VII may be used to infer the local scattering environment within the mixed-phase region of the convective cloud which, along with source height, has been shown in simulations to impact the amount of light emitted from cloud top (Brunner and Bitzer 2020). Data from the Maximum Expected Size of Hail (MESH) (Witt et al. 1998) product were also recorded to infer cloud optical depths of the convective updraft, which can correspond inversely with GLM optical energy measurements in severe thunderstorms and potentially impact data quality from the sensor (Calhoun et al. 2018). Last, the MRMS 0–2-km azimuthal shear product (Lakshmanan et al. 2006; Mahalik et al. 2019) (hereinafter AzShear) was collected for each supercell case study. Azimuthal shear has been used to diagnose low-level mesocyclones and tornadoes (Cintineo et al. 2020; Sandmæl et al. 2023) with values ranging from the 98th percentile to the maximum value within a storm. In this study, the 99th percentile and maximum values were sampled from each supercell.

Ground-based total lightning data (intracloud and cloud-to-ground flashes) from the Earth Networks Total Lightning Network (ENTLN) (Zhu et al. 2022) were compared against GLM storm-total flash rates. The ENTLN contains over 900 sensors across the CONUS (Zhu et al. 2017), with a reported DE of total lightning over the southern CONUS exceeding 70% (Rudlosky 2015) and exceeding 90% in areas with increased sensor density (Zhu et al. 2017). A 2021 processing upgrade to the network increased pulse detection across North America by 45%, with the largest observed improvements made over the oceans (Zhu et al. 2022).

Severe weather events from NOAA's *Storm Data* archive (Strassberg and Sowko 2021) were also included to provide verification of hazardous weather events associated with the ABI, GLM, and MRMS datasets. While reports of severe weather provide a number of caveats related to reporting biases, detection rates, and miscellaneous human factors (Kelly et al. 1985; Potvin et al. 2019; Trapp et al. 2006), their spatial and temporal references to severe weather occurrences were leveraged for this study with regard to severe hail (≥1 in.), wind (≥58 mph), and tornadoes.

c. Data processing

Data were collected for two case studies along with a bulk data study which expands upon the dataset created by Thiel et al. (2020). The two case studies featured discrete supercell thunderstorms from 24 May 2019 (southeastern Kansas) and 25 March 2021 (central Alabama) to provide a variety of supercell types, associated environments, hazards, and satellite viewing angles. Discrete supercells were selected for their ability to produce severe and high-impact phenomena such as large hail, damaging winds, and tornadoes, along with producing a quasi-steady updraft that could be studied with respect to its lightning, radar, and satellite signatures. The approximate GLM16 and GLM17 viewing angles of the 24 May 2019 supercell (from zenith) were 50° and 60°, respectively. In comparison, GLM16 and GLM17 viewing angles of the 25 March 2021 supercell (from zenith) were approximately 40° and 65°, respectively. The 1-min data from both GLM instruments were directly compared for the case studies, with MRMS data recorded every 2 min. Storm-total flash rates from both GLMs and the ENTLN were also accumulated over 5 min and updated every 1 min. Time series data were generated by manually tracking the supercell of interest and selecting the maximum GLM and MRMS values from the supercell.

ABI16, GLM16, and *Storm Data* information for the bulk study were collected using the same time period (13 April–31 May 2019) and 20-km target grid based on the *GOES-16* CONUS sector as Thiel et al. (2020). Additionally, ABI16 and GLM16 data were collected using the same KD-tree method to find the desired maximum or minimum value near each grid point. While Thiel et al. (2020) use preliminary local storm reports from the National Weather Service, quality-controlled events from *Storm Data* can combine multiple reports into one event with additional time and path information. Therefore, *Storm Data* events were linearly interpolated in space and time to improve their coverage in the bulk study. The number of marked samples when using the interpolated *Storm Data* events was nearly identical when compared against the preliminary local storm reports, which displayed the robust nature of a 15-km radius of influence and 10-min temporal window used by Thiel et al. (2020). The GLM and ABI data filters cited in Thiel et al. (2020) were also used in the current study, as adjustments in the GLM ground processing to remove false flashes in certain regions of the CONUS scene had not been made yet. These filters removed all data with cloud-top heights below 1 km as well as pixels that met all of the following conditions: 1) ABI cloud-top brightness temperatures greater than 270 K, 2) FED values greater than 10 flashes per 5 min, and 3) ABI cloud-top heights less than 4 km. The bulk dataset does keep flashes that have been artificially split in the GLM Lightning Cluster Filter algorithm (Goodman et al. 2012), which impacts approximately 3% of all recorded GLM flashes (Peterson 2019). However, these effects are minimal when interpreting a storm's maximum FED and minimum MFA, or assessing the bulk distributions of FED and MFA.

MRMS data from the original 0.01° grid were resampled using the bulk dataset's 20-km target grid through a modified KD-tree method (Maneewongvatana and Mount 1999). All MRMS points from the most recent available time step and within a 15-km radius of influence were selected from each point in the 20-km target grid, with the maximum value from

each MRMS variable then assigned to the grid point. The 15-km radius of influence was selected due to the decreasing resolution of the ABI CONUS scene from nadir, along with to mitigate horizontal displacement of satellite features due to parallax. A 10-km radius of influence would result in a substantial undersampling of values over a majority of the CONUS domain, while a radius of influence of 15 km created more normally distributed sampling errors when testing the KD-tree method. Additionally, the median parallax corrected distance across the central and eastern CONUS from the bulk dataset was approximately 12 km. To further increase the quality of MRMS observations with respect to the current density of the WSR-88D network across the CONUS, only MRMS values located east of 105°W were leveraged within the bulk dataset.

3. Supercell thunderstorm cases

a. 24 May 2019

On 24 May 2019, a stationary, longwave, upper-level trough extended across the western United States, with downstream ridging over the Ohio River valley. A stationary front was positioned between the ridge and trough axes over western Texas and central Kansas. Persistent moisture advection below the 850-hPa level from the Gulf of Mexico increased surface dewpoints to exceed 21°C across northern Oklahoma and 18°C in central and eastern Kansas at 1800 UTC. The 1800 UTC rawinsonde from Lamont, Oklahoma, highlighted increased convective instability with a mixed-layer convective available potential energy (ML-CAPE) value of 2005 J kg^{-1}, mixed-layer convective inhibition (ML-CIN) of -10.1 J kg^{-1}, and precipitable water (PWAT) of 49.24 mm (1.94 in.). Widespread instability, minimal inhibition, and 0–6-km bulk wind shear values exceeding 50 kt (1 kt $\approx$ 0.51 m s^{-1}) provided a suitable environment for widespread convection and the potential for supercell thunderstorms. Convection initiated along the stationary front in southern Kansas by 1600 UTC with thunderstorms becoming more widespread over the following six hours. A discrete thunderstorm initiated around 2000 UTC in Sumner County, Kansas, and continued to intensify into a supercell over the next 80 min until its first tornado report at 2119 UTC (Figs. 1 and 2).

Genesis of the updraft was identified at 2000 UTC, near Sumner County, in a region with adjacent convection ongoing to its north and larger GLM flashes propagating between these two regions. Local minima in MFA values at 2001 UTC exceeded 1200 and 2000 km^2 from GLM16 and GLM17, respectively, with maximum FED values of 18 flashes per 5 min from both sensors, while storm-total flash rates were exceptionally low. The maximum MRMS -10°C reflectivity value was greater than 40 dBZ at 2000 UTC and steadily increased over the proceeding 15 min to 49 dBZ, indicating a persistent updraft able to lift hydrometeors into the mixed-phase region. During this time, maximum values from the vertically integrated variables, MESH and VII, remained below 5 mm and 6 kg m^{-2}, respectively, and FED increased to 47 flashes per 5 min for both GLMs. The local MFA minima decreased to

422 km^2 from GLM16 and 301 km^2 from GLM17 between 2001 and 2015 UTC. Maximum observed TOE values from GLM16 during this time decreased from 988 to 195 fJ; however, GLM17-TOE observed a prominent spike at 2008 UTC of 2545 fJ before decreasing to 341 fJ at 2015 UTC.

At 2030 UTC, GLM16-FED increased rapidly from 44 to 73 flashes within 1 min and was matched by a decrease in the MFA from 636 to 71 km^2. However, GLM17-FED remained constant during this period and corresponding MFA values decreased from 302 to 150 km^2. TOE values from both GLMs also increased but with different magnitudes. From GLM16, TOE values increased from 562 to 923 fJ between 2028 and 2031 UTC, while TOE from GLM17 increased from 794 to 1822 fJ between 2028 and 2032 UTC. The increased intensity across all three recorded GLM gridded variables around 2030 UTC coincided with the onset of rising values across all four MRMS variables and preceded an increase in ENTLN flash rates at 2040 UTC. Around 2040 UTC, the storm of interest also deviated right of the mean storm motion and developed forward and rear flank downdrafts along with a consistent overshooting top signature, indicative of a maturing supercell thunderstorm.

During the next 20 min, from 2040 to 2100 UTC, the gridded GLM values remained steady while the MRMS variables steadily increased. MRMS MESH, VII, and -10°C reflectivity during this 20-min period increased from 12 to 29 mm, from 13 to 40 kg m^{-2}, and from 53 to 63 dBZ, respectively, indicating an increasing number of large hydrometeors were lofted by the supercell's updraft to higher altitudes, including the mixed-phase region. Maximum AzShear values suddenly increased between 2102 and 2014 UTC from 0.012 to 0.020 s^{-1}, the largest value of the entire case. Also, during this period, GLM16 consistently recorded greater maximum FED values and total flash rates by approximately 25 flashes than GLM17, while maximum TOE values from GLM17 were approximately 200 fJ brighter than those from GLM16. Over the proceeding 15 min from 2100 to 2115 UTC, maximum FED values remained elevated from both GLMs, while minimum MFA values decreased from 283 to 71 km^2 from GLM16, and from 226 to 76 km^2 from GLM17. At this time, both local minima in MFA values were at their smallest possible areas from their respective sensor at their current viewing angles. Maximum TOE values from both sensors increased during this time, with GLM16-TOE increasing from 455 fJ at 2100 UTC to 1073 fJ at 2111 UTC and GLM17-TOE increasing from 828 to 1520 fJ.

The maximum values of MESH, VII, and -10°C reflectivity increased to exceed 40 mm, 60 kg m^{-2}, and 60 dBZ, respectively, between 2100 and 2120 UTC. At 2119 UTC, a tornado was spotted south of Douglass, Kansas, and two instances of wind damage in Douglass were reported. FED and MFA values remained consistent during the onset of the severe weather, while TOE values from both GLMs fell below 500 fJ. Conversely, all three MRMS reflectivity products continued to increase, achieving their maximum values in the case between 2125 and 2130 UTC. Hail of 1 in. was reported at 2140 UTC west of Leon, Kansas, and another tornado report was received at 2153 UTC as maximum FED values from GLM16

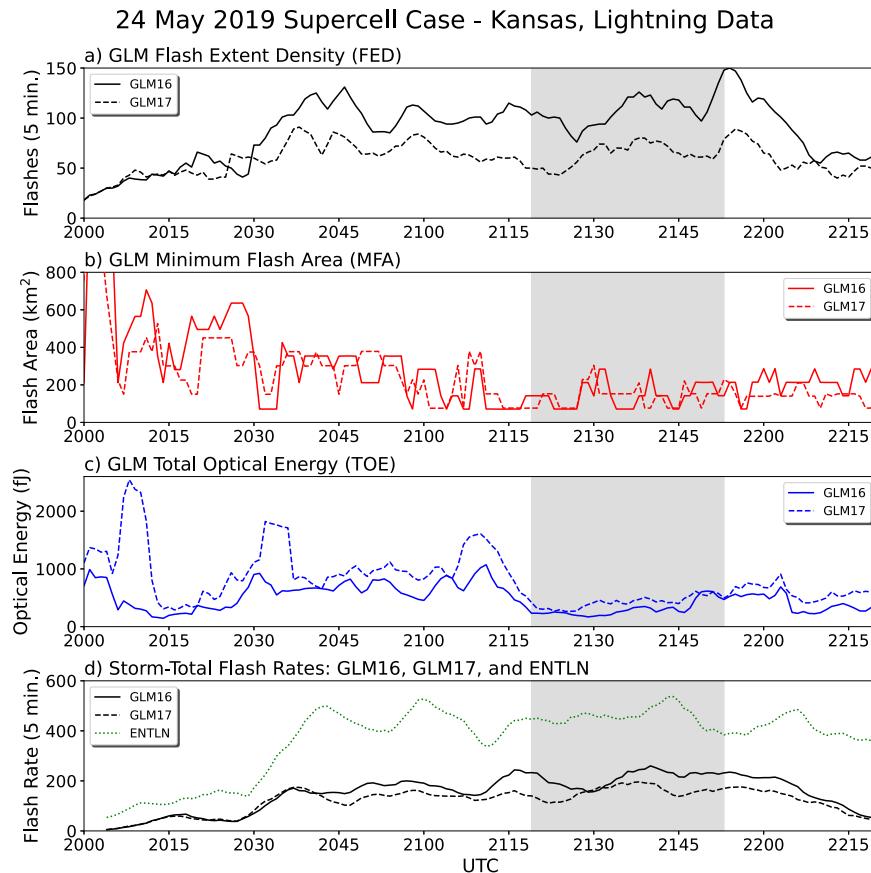## 24 May 2019 Supercell Case - Kansas, Lightning Data

FIG. 1. Time series plots from the 24 May 2019 supercell case in Kansas, including the gridded *GOES-16* and *GOES-17* GLM (GLM16 and GLM17) variables: (a) flash extent density, (b) minimum flash area, (c) total optical energy, and (d) 5-min flash rates from the GLM16, GLM17, and ENTLN. The gray bar in each panel represents the time between the first and last storm reports associated with the supercell.

and GLM17 reached 150 and 89 flashes shortly thereafter. After the second tornado report, total flash rates from both GLMs decreased as the supercell weakened and merged with nearby convection. Through the entire 140-min lifespan of the storm, GLM16 observed 26% more flashes than GLM17. Conversely, GLM17 observed 57% more optical energy than GLM16, resulting in GLM17 observing almost twice as much optical energy per flash when compared to GLM16.

b. 25 March 2021

A midlevel, shortwave trough crossed from the southern Plains to the Great Lakes region on 25 March 2021 and coincided with a deepening midlatitude cyclone across Arkansas and western Tennessee. At 1200 UTC, a 50-kt lower-tropospheric jet at 850 hPa across Mississippi and Alabama advected lower-tropospheric moisture from the Gulf of Mexico into the region. Surface dewpoints across central Mississippi and southern Alabama exceeded 18°C behind a diffuse surface warm front, with a cold front positioned across western Texas and a broad stationary front extended from northern Louisiana through the Ohio River valley region. Rawinsonde observations at 1500 UTC from the Jackson, Mississippi, upper air site, within the warm

sector of the cyclone, continued to show a lower-tropospheric jet up to 55 kt centered at 750 hPa. ML-CAPE, ML-CIN, and PWAT values of 2184 J kg^{-1}, −2.91 J kg^{-1}, and 35.75 mm (1.41 in.), respectively, were observed, and 0–6-km bulk shear exceeded 60 kt with strong lower-tropospheric shear. This created an environment conducive to semidiscrete supercells capable of producing tornadoes spanning from central Mississippi and Alabama to southern Tennessee. At 1500 UTC, a line of semidiscrete convection initiated along a prefrontal band stretched from southeast Mississippi to northwest Alabama, moving northeast into a region with increasingly backed surface winds. Convection along this line became more discrete over the proceeding hour, with one discrete thunderstorm of note east of Meridian, Mississippi, along the Alabama–Mississippi border at 1600 UTC. This thunderstorm continued to intensify and develop into a supercell thunderstorm by 1630 UTC in Sumter County, Alabama, which produced three tornadoes across Alabama over the proceeding 4 h (Figs. 3 and 4).

At 1630 UTC, the supercell had maximum FED values of 31 flashes from GLM16 and 26 flashes from GLM17. Isothermal reflectivity values at −10°C exceeded 50 dBZ, with MESH and VII values at 7 mm and 18 kg m^{-2}, respectively.

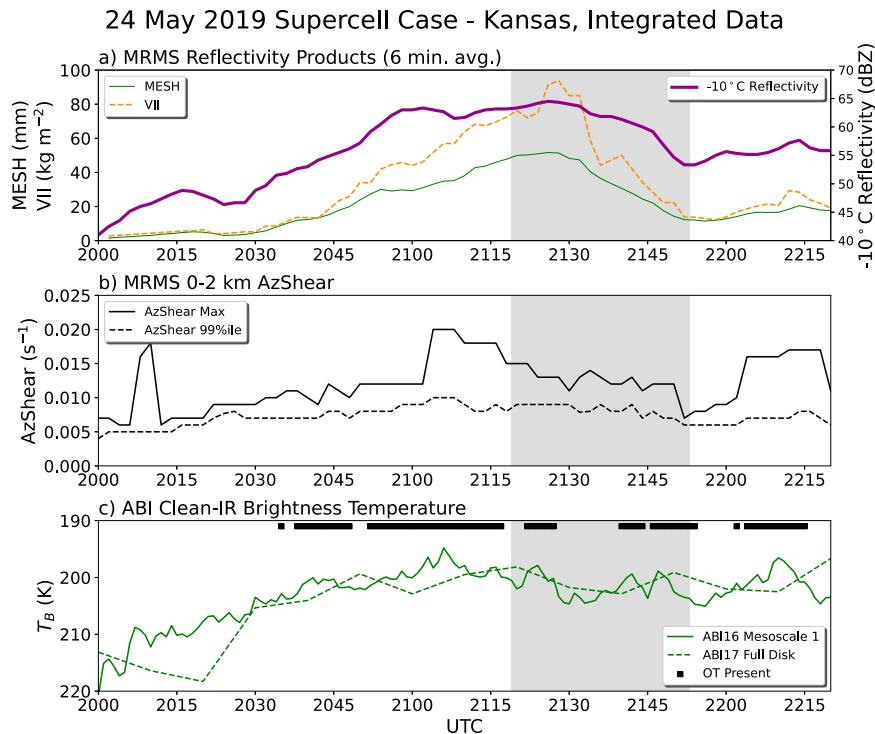### 24 May 2019 Supercell Case - Kansas, Integrated Data

FIG. 2. As in Fig. 1, but with (a) MRMS reflectivity products, (b) MRMS 0–2-km azimuthal shear, and (c) ABI clean-IR brightness temperatures from the available ABI16 and ABI17 scenes along with overshooting top (OT) identification.

Maximum TOE values from GLM17 (259 fJ) were initially 3 times greater than the maximum recorded by GLM16 (80 fJ). TOE from GLM17 increased between 1639 and 1645 UTC from 300 to 1110 fJ, while TOE from GLM16 only increased from 100 to 158 fJ. Then, 15 min later at 1701 UTC, the maximum TOE from GLM17 rapidly increased again to 1997 fJ, while the maximum TOE from GLM16 was only 284 fJ. The second increase in GLM17-TOE at 1653 UTC coincided with increased FED values, along with increased total flash counts from both GLMs and the ENTLN. A few minutes later around 1700 UTC, MESH, VII, and maximum AzShear began to steadily increase with the emergence of an overshooting top signature, indicating a strengthening updraft capable of lofting larger hydrometeors into the mixed-phase region with an organized low-level mesocyclone. Storm-total flash rates from GLM16 continued to increase after 1700 UTC, while flash rates from GLM17 slowly decreased with a reduced optical signal to the sensor as observed in lower TOE values. Consequently, GLM16-FED remained over 100 flashes, while GLM17-FED decreased to approximately 50 flashes by 1710 UTC.

At approximately 1718 UTC, the supercell produced its first tornado in northern Hale County as the maximum AzShear exceeded 0.03 s^{-1}, and achieved its peak value for the case of 0.036 s^{-1} at 1722 UTC. While the tornado was on the ground for approximately 16 min, FED from GLM16 and GLM17 initially decreased until 1725 UTC. After 1725 UTC, GLM16-FED increased from 61 to 126 flashes at 1742 UTC, while GLM17-FED increased from 30 to 131 flashes. During

the same time period, GLM17-TOE showed a third rapid increase from 253 to 2530 fJ, while maximum GLM16-TOE values increased from 215 to 608 fJ. The second tornado began at approximately 1752 UTC in northern Bibb County as the maximum AzShear value began to rise less the 10 min prior. Maximum FED, maximum TOE, and total flash rates from GLM16 and GLM17 decreased from 1742 to 1830 UTC and stayed at these lower values through 1900 UTC. The second tornado dissipated around 1908 UTC in extreme southern St. Clair County.

Around 1900 UTC, 8 min before the second tornado ended, the parent updraft supporting the mesocyclone appeared to dissipate as a new updraft formed along its rear flank. Isothermal reflectivity at −10°C rapidly increased from 48 to 59 dBZ by 1912 UTC, and in response, MESH and VII also increased to 18 mm and 20 kg m^{-2}, respectively, by 1916 UTC. As more hydrometeors were lofted into the mixed-phase region, GLM16 and ENTLN observed increasing flash rates while GLM17 recorded little change. Flash rates continued to increase across the three lightning location systems until genesis of the third tornado at 1932 UTC, just after the maximum AzShear value peaked at 0.03 s^{-1} again. Less than 10 min prior to tornadogenesis was the only instance where flash rates from GLM17 increased slightly in tandem with GLM16 and ENTLN. All three MRMS variables also remained elevated until the end of the third tornado at 2026 UTC. Through the 270-min study of the supercell, GLM16 recorded 168% more flashes than GLM17. When accumulating the
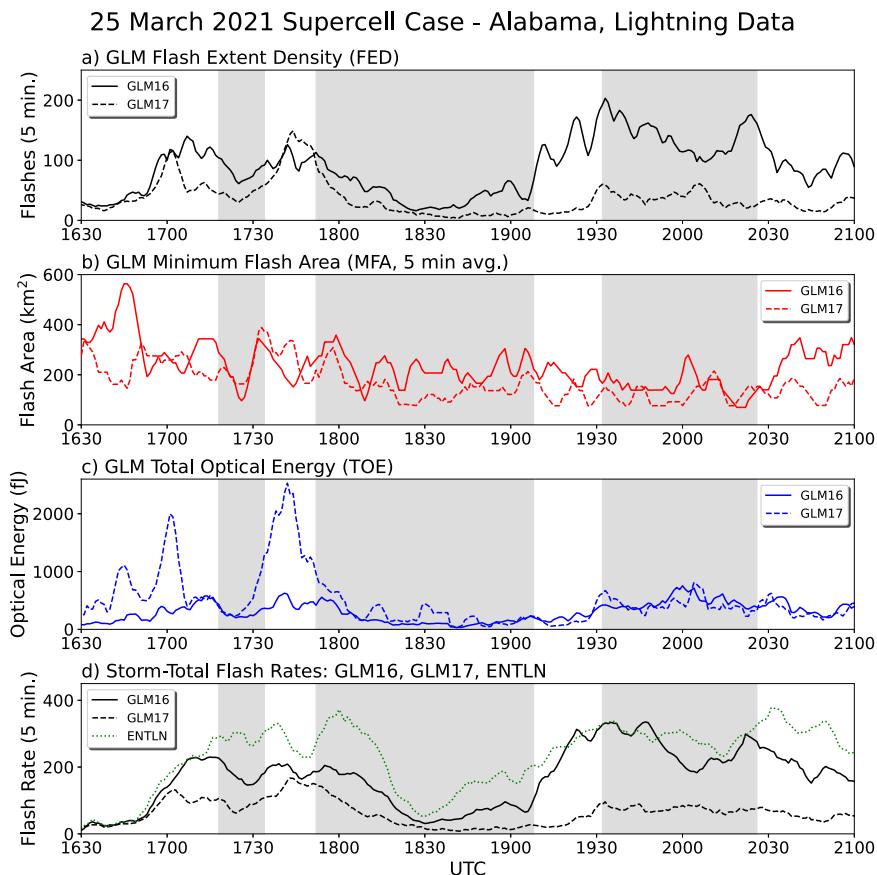
FIG. 3. Time series plots from the 25 Mar 2021 supercell case in Alabama, including the gridded *GOES-16* and *GOES-17* GLM (GLM16 and GLM17) variables: (a) flash extent density, (b) minimum flash area, (c) total optical energy, and (d) 5-min flash rates from the GLM16, GLM17, and ENTLN. The gray bars in each panel represent the estimated time periods that the supercell was producing a tornado (estimated from NWS surveys and MRMS data).

optical energy from all of the flashes from each sensor, GLM16 recorded 27% more optical energy than GLM17, which means that GLM17 observed 112% more optical energy per flash than GLM16.

4. GLM, ABI, and MRMS bulk data intercomparisons

Over the 7-week period of study, 2.8 million instances of gridded GLM data were collocated with ABI and MRMS information across the central and eastern United States (Fig. 5). Intercomparisons were largely limited to the continental United States due to the spatial extent of the WSR-88D network used by the MRMS system. Samples were most frequently located in the Central Plains with a local maximum in southeast Kansas and broad regions exceeding 600 samples existed across the Central and Southern Great Plains.

Triple-sensor intercomparisons between ABI clean-IR cloud-top brightness temperatures (hereinafter referred to as brightness temperatures), gridded GLM variables, and the MRMS isothermal reflectivity at −10°C in Fig. 6 provided a unique perspective of convection across the three platforms with over 1.89 million samples. The 2D histogram in Fig. 6a, binned every

1 K and 1 dBZ, was used to examine the relationship between brightness temperature and isothermal reflectivity with respect to flashes recorded by the GLM. Flashes occurred at a variety of brightness temperatures and reflectivity values between 190 and 260 K and from 10 to 65 dBZ, respectively. GLM flashes most frequently occurred between brightness temperatures of 200–230 K and reflectivity values of 20–50 dBZ, with this region containing 50.2% of all samples in the bulk dataset. Median GLM values were sampled from the binned data in Fig. 6a to assess trends in the gridded variables as a function of brightness temperature and isothermal reflectivity. Binned, median FED values in Fig. 6b display a dependence on brightness temperature when isothermal reflectivity values were less than 30 dBZ. In this region, FED values increased from less than 2 flashes per 5 min at brightness temperatures greater than 240 K to FED values greater than 10 and 20 flashes for brightness temperatures less than 205 and 200 K, respectively. At isothermal reflectivity values greater than 30 dBZ, decreasing brightness temperatures and increasing isothermal reflectivity values correspond to greater FED values. Brightness temperatures below 210 K and isothermal reflectivity values above 50 dBZ correspond with FED values greater than
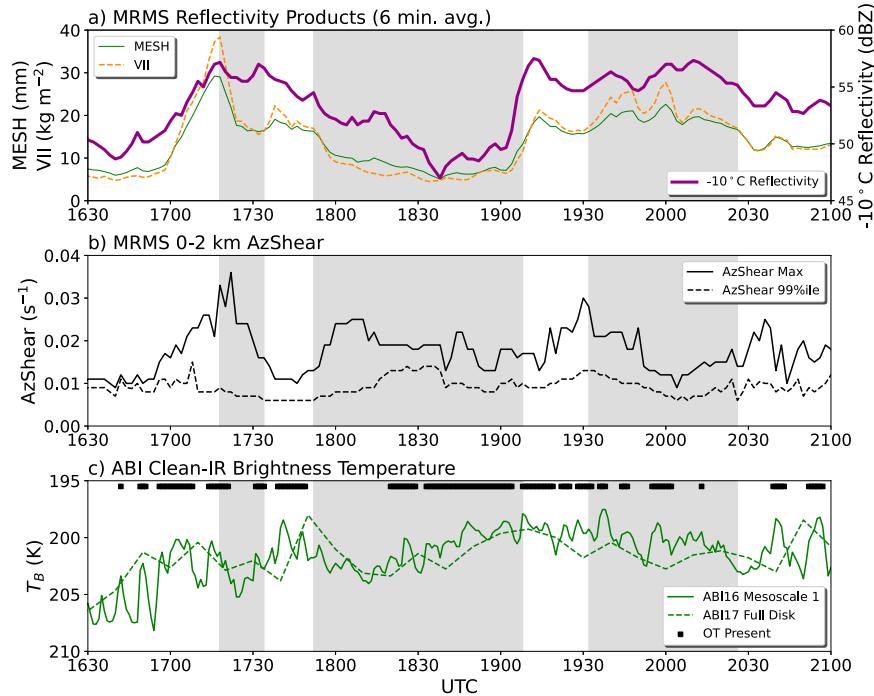
FIG. 4. As in Fig. 3, but with (a) MRMS reflectivity products, (b) MRMS 0–2-km azimuthal shear, and (c) ABI clean-IR brightness temperatures from the available ABI16 and ABI17 scenes along with overshooting top (OT) identification.

20 flashes per 5 min, indicating the presence of robust updrafts which generated more frequent local flash rates. FED values dramatically increase with brightness temperatures less than 200 K, exceeding 40 flashes across nearly all isothermal reflectivity values.

Variations in the median MFA values in each bin from Fig. 6c also exhibit a strong dependence on brightness temperature when isothermal reflectivity values are below 30 dBZ, similar to Fig. 6b. However, there is an observed peak in MFA exceeding 500 km^2 between brightness temperatures from 210 to 230 K and isothermal reflectivity values from 20 to 30 dBZ. Median MFA values then slowly decrease to between 300 and 400 km^2 within this reflectivity range as the brightness

FIG. 5. Location density values for all GLM-MRMS samples within the 7-week period of study from 13 Apr to 31 May 2019.

temperature increases to 240 K. Conversely, decreasing brightness temperatures after this peak around 220 K correspond with MFA values decreasing to their smallest possible values below 100 km^2. For samples exceeding 30 dBZ, increasing isothermal reflectivity and decreasing brightness temperature corresponded with decreasing minimum flash areas. Median TOE values in Fig. 6d did not exhibit similar relationships as in Figs. 6b and 6c. Across all isothermal reflectivity values, TOE exhibited a strong dependence on brightness temperature. A subtle maximum in TOE was observed between 25 and 35 dBZ coinciding with the peak in MFA in Fig. 6c. The greatest median TOE values exceeding 60 fJ occur at brightness temperatures below 200 K and isothermal reflectivity values greater than 35 dBZ, which corresponded to the greater FED values in Fig. 6b as more flashes contributed to the accumulated optical energy observed. Median TOE values exceeding 20 fJ typically occurred at brightness temperatures below 210 K; however, between isothermal reflectivity values of 25 and 35 dBZ, this contour increased to brightness temperatures of nearly 220 K at 30 dBZ.

While Fig. 6 broadly defined how ABI clean-IR brightness temperature and MRMS isothermal reflectivity at −10°C correspond to all gridded GLM variables, samples that coincided spatially and temporally with *Storm Data* events provided additional insight into these interrelationships with respect to severe convection. The 2D histogram of all forty-four thousand points in Fig. 7a reflects a shift in the proportion of samples to colder brightness temperatures and greater isothermal
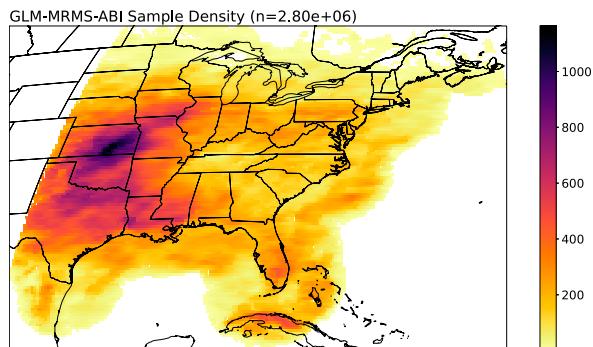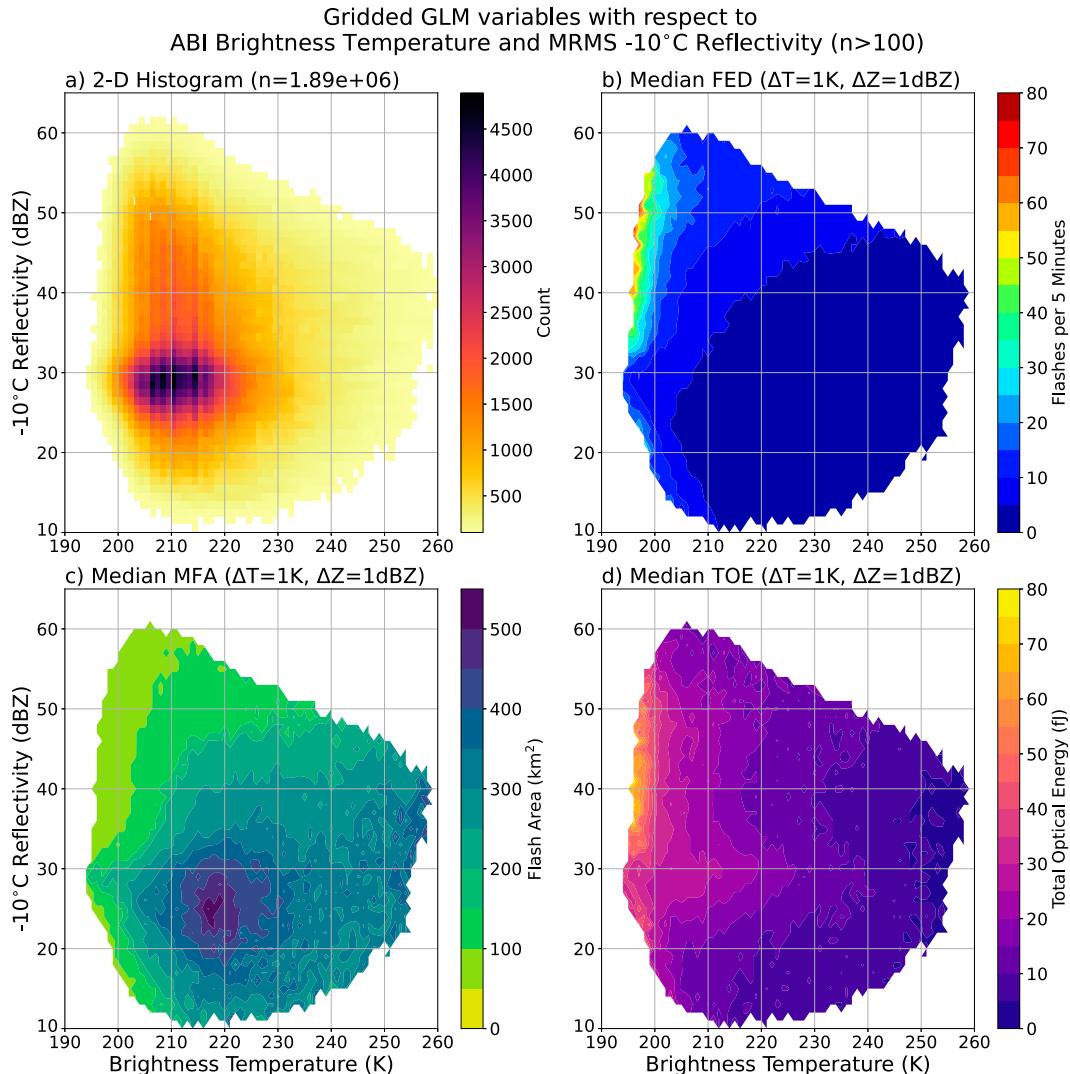
FIG. 6. Gridded GLM variables compared to ABI clean-IR brightness temperature and MRMS −10°C reflectivity. (a) The distribution of sampled GLM pixels, with the false flash filter applied, when binned by ABI brightness temperature every 1 K and MRMS −10°C reflectivity every 1 dBZ. Median (b) FED, (c) MFA, and (d) TOE values sampled from the bins used in (a). (Median calculation requires a minimum of 100 samples.)

reflectivity values when compared to Fig. 6a. Most samples are concentrated at brightness temperatures from 200 to 220 K and isothermal reflectivities from 25 to 60 dBZ. A peak in samples at a brightness temperature of 205 K and isothermal reflectivity of 50 dBZ is 5 K colder and 20 dBZ greater than the approximate peak in samples in Fig. 6a. When coinciding with severe weather occurrence, median FED and MFA values depict a strong dependence on brightness temperature across all isothermal reflectivities (Figs. 7b,c). MFA values below 100 km^2 at brightness temperatures below 210 K highlight an overall warmer threshold than similar MFA contours in Fig. 6c. FED and MFA still show a prominent inverse relationship, especially for the peak in MFA values exceeding 300 km^2 from 25 to 30 dBZ and from 215 to 220 K. Trends in median TOE values in Fig. 7d were difficult to identify, with exception to a general dependence on brightness temperature similar to the

median FED and MFA contours in Figs. 7b and 7c. Overall, the greatest median TOE values (exceeding 30 fJ) occurred at brightness temperatures less than 205 K.

Distributions of the sampled MRMS MESH and VII values within the bulk dataset resemble exponential distributions. Thus, violin plots (Figs. 8 and 9) provide distributions of gridded GLM values as functions of discrete MESH and VII bins. FED distributions within the MESH bins (Fig. 8a) reveal an initial increase in FED as MESH increases; however, for MESH values greater than 20 mm, the distributions show little change. MESH values less than 10 mm peak in the distribution around 3 flashes per 5 min, with the median value of 8 flashes and 75th percentile value of 20 flashes. The 10–20-mm bin displays an increase in these values, with a peak in the distribution closer to 6 flashes, along with median and 75th percentile values of 14 and 38 flashes, respectively. All successive distributions
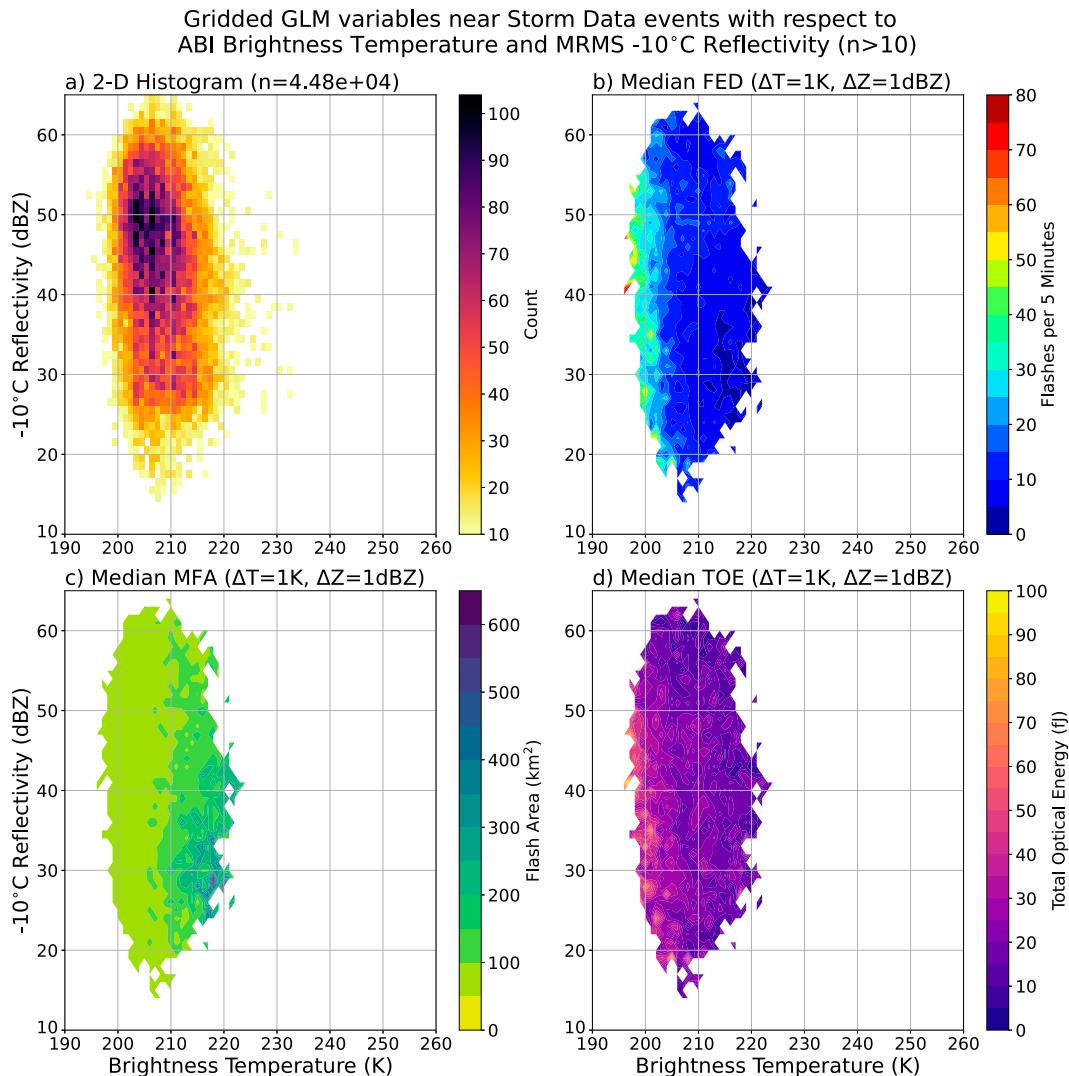
Gridded GLM variables near Storm Data events with respect to
ABI Brightness Temperature and MRMS -10°C Reflectivity (n>10)

FIG. 7. Gridded GLM variables compared to ABI clean-IR brightness temperature and MRMS $-10°$C reflectivity near local storm reports. (a) The distribution of sampled GLM pixels, with the false flash filter applied, when binned by ABI brightness temperature every 1 K and MRMS $-10°$C reflectivity every 1 dBZ. Median (b) FED, (c) MFA, and (d) TOE values sampled from the bins used in (a). (Median calculation requires a minimum of 10 samples.)

contain peaks around 10 flashes per 5 min, with median values between 10 and 20 flashes and 75th percentile values between 25 and 40 flashes. MFA distributions in Fig. 8b show an inverse trend to the FED distributions, with flash areas decreasing initially with increasing MESH size. MFA values were consolidated around 150 km^2 (two GLM pixels) when MESH was less than 10 mm, and decrease to less than 100 km^2 (one GLM pixel) for all MESH bins greater than 10 mm. One ubiquitous aspect across all MESH bins is that peaks in the frequency distributions occur at the size of a single GLM pixel, showing that convection capable of producing hail often coincided with the smallest possible GLM flashes. While FED and MFA showed distinct trends across the various MESH bins, TOE distributions in Fig. 8c present no discernible signals in the median, 25th percentile, and 75th percentile values.

Gridded GLM and VII samples were binned every 5 kg m^{-2} for the first two bins and every 10 kg m^{-2} afterward. These distributions with respect to VII in Fig. 9a show an initial increase in the lowest VII bins similar to those observed in Fig. 8a. Median and 75th percentile FED values increase across the lowest two VII bins ($<$5 kg m^{-2} and 5–10 kg m^{-2}) from 4 to 11 kg m^{-2} and from 12 to 27 kg m^{-2}, respectively. Moving to successively greater VII bins, the distributions again show little variations with median values of approximately 12 kg m^{-2} and 75th percentile values between 30 and 40 kg m^{-2}. MFA and TOE distributions in Figs. 9b and 9c also show similar results to those found in Figs. 8b and 8c, respectively. Trends in MFA distributions are inversely proportional to those represented in the FED distributions, especially when inspecting the decreasing MFA values at the median and 75th percentile as the VII bins increased. TOE has little to no variations across the six discrete VII bins, with only slight differences between the 75th percentile TOE values.
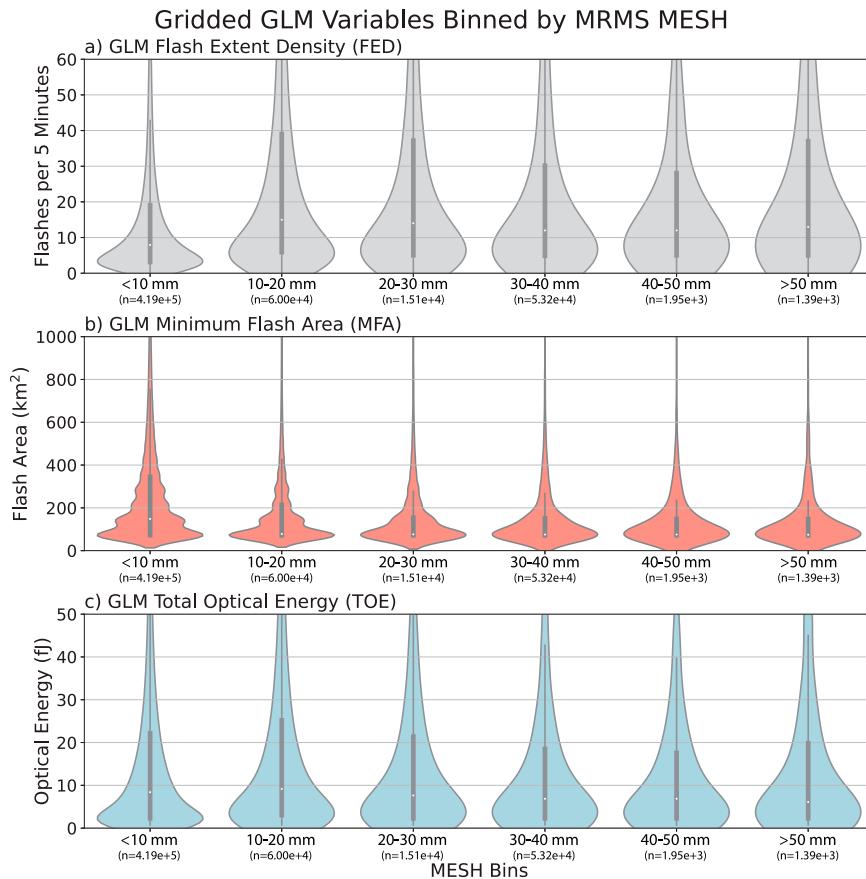
FIG. 8. Distributions of the gridded GLM variables (a) FED, (b) MFA, and (c) TOE binned with respect to their corresponding MESH values every 10 mm.

5. Discussion

a. GLM data fusion applications

GLM flash extent density corresponded inversely to local flash area in both supercell case studies and the larger 7-week study. Decreases in flash area, as reported from the local minima in MFA, for each supercell case (Figs. 1 and 3) coincided with increasing maximum FED values and storm-total flash rates from the GLM16, GLM17, and ENTLN. The inverse relationship between local flash rates and areas was readily observed in the bulk study when the median, gridded GLM variables were plotted with respect to binned MRMS $-10°$C isothermal reflectivities and ABI clean-IR brightness temperatures (Fig. 6). For samples that coincided with severe convection (Fig. 7), the inverse flash rate to flash area relationship persisted. Additionally, when binned by MRMS VII and MESH, FED and MFA presented relatively high and low values, respectively, when MESH exceeded 20 mm and VII exceeded 10 kg m^{-2}. The inverse relationship between local flash rate and area observed in the case studies and bulk study supports the results from previous studies (Bruning and Mac-Gorman 2013; Calhoun et al. 2013; Schultz et al. 2015). Elevated $-10°$C isothermal reflectivity values, often exceeding 30 dBZ, can signal active charge separation within intensifying

or robust convective updrafts (Buechler and Goodman 1990; Hondl and Eilts 1994; Mosier et al. 2011).

During the 24 May 2019 supercell case, updraft intensification at 2030 UTC from the GLM16 and GLM17 FED and MFA values marked the onset of increasing trends from MRMS MESH, VII, and isothermal reflectivity. When considering the ambient deep-layer shear and unstable thermodynamic environment, this signaled the thunderstorm had transitioned into a supercell. Onset of the rightward deviation of storm motion from the mean wind, noted at 2040 UTC, was driven by the linear dynamic pressure perturbation of the mesocyclone (Rotunno and Klemp 1982; Bunkers et al. 2000; Flournoy et al. 2021). Increasing lightning activity during this period of mesocyclogenesis further supports the observations from a majority of supercells observed by Stough et al. (2017) and shows that pairing MRMS isothermal and vertically integrated reflectivity products with GLM gridded imagery can provide complementary information for thunderstorm morphology and subsequent trends in severity potential.

Environments conducive to larger GLM flashes were also observed using the binned ABI brightness temperature and MRMS $-10°$C isothermal reflectivity in Fig. 6, which exhibited a peak in MFA values between isothermal reflectivity values of 20–30 dBZ and brightness temperatures of 210–230 K.
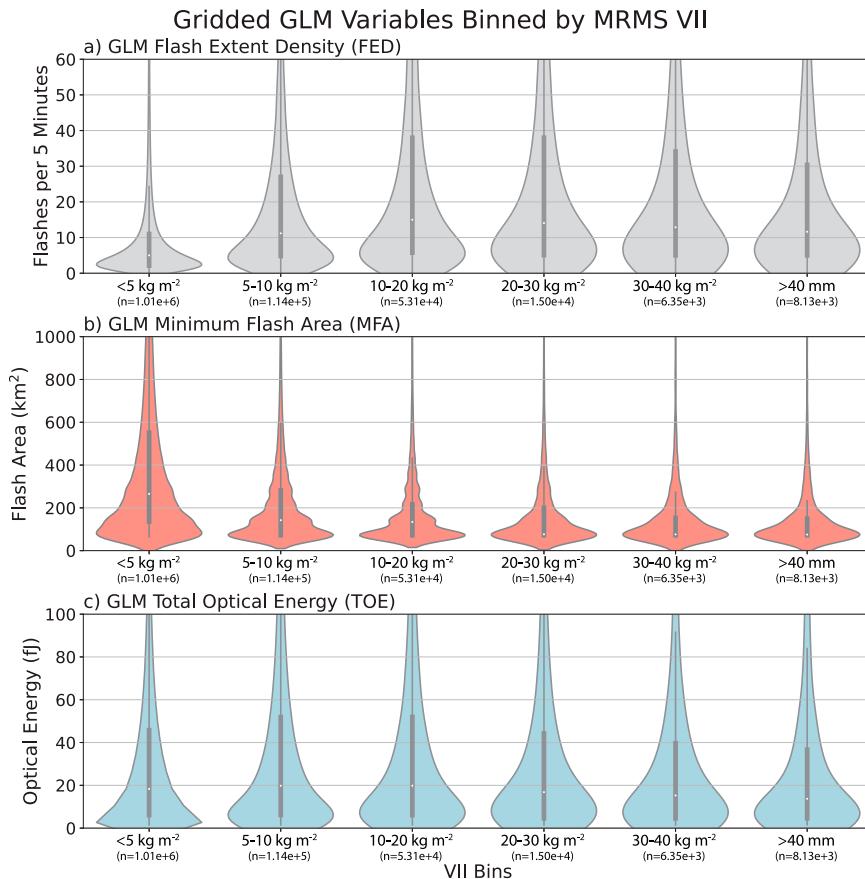
FIG. 9. Distributions of the gridded GLM variables (a) FED, (b) MFA, and (c) TOE binned with respect to their corresponding VII values every 5 kg m^{-2} below 10 kg m^{-2} and every 10 kg m^{-2} for values greater than 10 kg m^{-2}.

The combination of large flash areas with relatively low flash rates suggests that these scenarios contained a greater proportion of flashes which propagated through regions of stratiform precipitation supportive of local charge separation. Mecikalski and Carey (2018) showed from a sample of 27 mesoscale convective systems that a greater proportion of flashes were shown to propagate through regions of MRMS three-dimensional reflectivity between 20 and 30 dBZ, indicating an overall preference to larger, stratiform flashes within these reflectivities. While the reflectivity values sampled in the bulk study are restricted to the $-10°$C isothermal layer, the larger spatial footprint of lightning flashes provided by the GLM shows that a majority of flashes between isothermal reflectivity values of 20–30 dBZ and brightness temperatures of 210–230 K were associated with stratiform flashes. Operationally, a forecaster could use these values to highlight regions with the potential for large flashes that can expose the public to excessive lightning risk.

One additional caveat to this analysis can be found at the beginning of the 25 May 2019 supercell case study. MFA values from the storm exceeded 800 km^2 and coincided with ABI brightness temperatures between 210 and 220 K along with isothermal reflectivity values between 40 and 45 dBZ. Ongoing convection was noted near the storm of interest, with anvil regions from decaying convection present to the west and within 5 km identified from ABI16 brightness temperature data. Local charging within these anvil regions, and the presence of large flashes beyond the existing footprint of the developing storm, may have initiated in part due to interactions with the developing storm or from local initiation within the anvil as noted in Kuhlman et al. (2009) and Weiss et al. (2012). Because large, stratiform flashes can initiate in a variety of convective environments, the operational need to identify these electrified regions within stratified reflectivity and infrared brightness temperature regions remains a necessary area of study.

Gridded GLM products from the current study were evaluated in NOAA's Hazardous Weather Testbed–Experimental Warning Program (Calhoun et al. 2021). FED and MFA consistently received recommendations for operational implementation (Thiel and Calhoun 2021; Thiel 2022). The TOE product has been considered; however, specific applications within the context of short-term convective forecasting have been met with uncertainty by HWT participants (Thiel 2022). The qualitative feedback from the testbed was observed quantitatively in the presented study, as TOE did not present robust interrelationships with ABI, MRMS, and the other
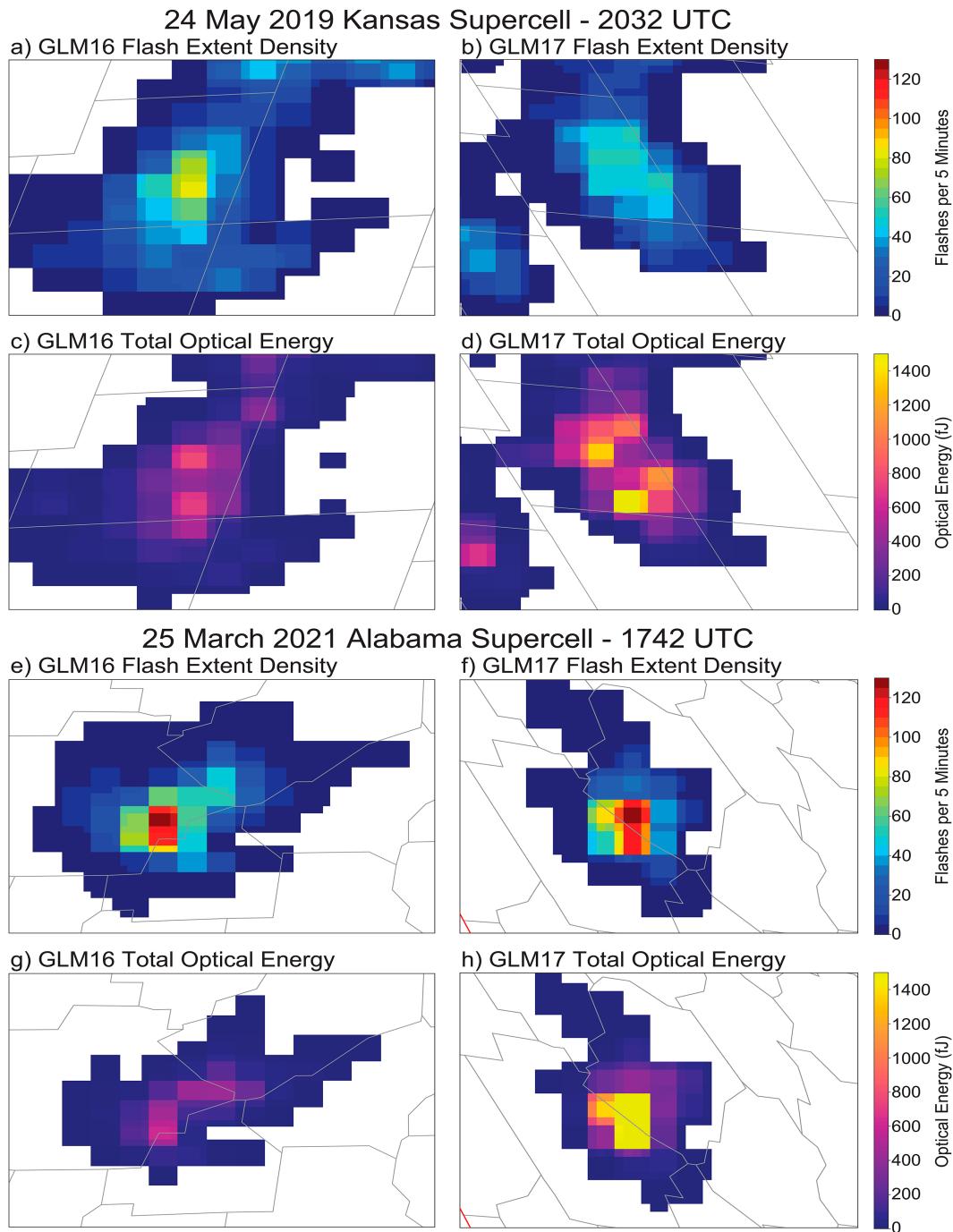
FIG. 10. Snapshots of GLM (a),(b),(e),(f) flash extent density and (c),(d),(g),(h) total optical energy for two case studies from 24 May 2019 and 25 Mar 2021 from the perspective of *GOES-16* (75°W) and *GOES-17* (137°W).

GLM variables within the study. Within the bulk study, trends in TOE did not correspond well with isothermal reflectivity in Figs. 6 and 7 but did with respect to cloud-top brightness temperature. One possible explanation for these poor relationships is that the observed optical energy from a lightning flash varies with respect to not only the optical properties of the ambient convective cloud (Brunner and Bitzer 2020; Peterson 2020) but also the emitting properties of the lightning channels themselves (Thomas et al. 2000; Petersen and Beasley 2013). This presents considerable challenges for operational implementation of TOE, as HWT participants have shown reduced confidence and perceived utility in TOE when compared to FED and MFA (Thiel and Calhoun 2021; Thiel 2022).

b. Dual-GLM observations

During both supercell cases, GLM16 observed greater storm-total and localized flash rates than GLM17 overall. However, the ratio of GLM16 to GLM17 flash rates varied temporally, with periods in both cases where GLM17-FED values exceeded those from GLM16. This occurred even at greater GLM17 viewing angles such as the 25 March 2021 case in the southeastern CONUS. Bateman et al. (2021) found average GLM16 detection efficiencies exceeded 70% in the southeastern, south central, and central CONUS regions, while GLM17 values were often below 50% in the southeastern CONUS and between 50% and 70% in the south and central CONUS regions. Rudlosky and Virts (2021) demonstrated relative differences in local GLM flash rates between GLM16 and GLM17 in the region of sensor overlap. In the southeastern CONUS, GLM16 observed nearly all of the flashes detected by GLM17, which observed approximately 50% of all GLM16 flashes. GLM16 also observed slightly more flashes in the central and southeastern CONUS regions than GLM17. Therefore, in both case studies presented, GLM16 should observe more flashes than GLM17. This expectation was met throughout each case, with exception to times when the supercells intensified.

When GLM17-FED exceeded GLM16 values during the 24 May 2019 case between 2020 and 2030 UTC (Fig. 1), storm-total flash rates increased, MFA values decreased, and maximum TOE values from GLM17 increased to become almost twice as great as those from GLM16 by 2032 UTC. In the bulk study, increased FED frequently corresponded with increasing TOE near severe weather and all cases (Figs. 6 and 7). However, there was a discrepancy when examining the FED and TOE imagery at 2032 UTC (Figs. 10a–d) where GLM17 observed greater TOE values in an area where GLM16 observed greater FED. As discussed previously, the GLM intensification signature signaled the onset of a mature supercell with a robust updraft and mesocyclone. Comparably, the 25 March 2021 supercell case also contained a period where local maxima in GLM16-FED and GLM17-FED were comparable (Figs. 10e–h), where GLM17 observed considerably greater TOE. MFA values also decreased just after 1730 UTC in Fig. 3, and there was a greater disparity in maximum TOE values between GLM16 and GLM17 while their storm-total flash rates became comparable. This occurred before the second reported tornado in the case, along with over 30 min earlier before the first tornado. Both supercell storms, while viewed from considerably different GLM viewing angles and convective environments, presented different indicators of intensification. GLM17 observed greater optical energy signatures from greater TOE values, but only when the instrument had a direct view of the side of the intensifying updraft. Because GLM16 was in a more favorable position for flash detections than GLM17, the instrument still had greater FED values and storm-total flash rates than GLM17.

The two case studies provide instances of anomalous GLM16-to-GLM17 activity when compared to the bulk statistics provided by Bateman et al. (2021) and Rudlosky and Virts (2021) and show that the quality of GLM observations is impacted by the propagation of visible and near-infrared light originating from each lightning flash through a convective cloud. Previous studies using Monte Carlo simulations and Boltzmann transport theory to characterize the propagation of photons through a convective cloud have shown that the vertical and horizontal position of the simulated optical source provides the largest effect on the amount of light that escapes from the top and sides of the convective cloud (Thomson and Krider 1982; Light et al. 2001; Brunner and Bitzer 2020; Peterson et al. 2020). Brunner and Bitzer (2020) found that while changes in the size distributions of cloud droplets and ice particles more greatly influenced optical emission than the concentration of the particles, the optical source height provided the largest impact on the amount of light that reached cloud top. This was especially apparent for source heights below 7 km. In supercell thunderstorms, Bruning and MacGorman (2013) showed that a greater number of flashes can occur upshear of the updraft. For both supercell thunderstorms studied, GLM17 had a more direct view of the flashes coinciding with each supercell's updraft due to its western perspective in these semidiscrete cases. This suggests that in certain scenarios with discrete updrafts in regions of moderate westerly shear, the GLM17 instrument may be able to capture more of the small flashes on the upshear side with higher optical radiances that help characterize updraft intensity trends.

Overall detection efficiencies from the GLM in the GOES-East position are still greater than overall in the south central, central, and southeastern CONUS regions than from the GOES-West GLM. However, both case studies suggest that the additional perspective from the GOES-West position may provide useful lightning information in short-term convective forecasting, specifically related to rapid increases in updraft speed and volume prior to severe weather occurrence (Schultz et al. 2015, 2017). Total optical energy in particular appeared to be most useful when assessing temporal changes in GLM DE from both supercells, and additional dual-GLM studies are needed to confirm the consistency and predictive value of this TOE signature. During the 2022 Satellite Proving Ground, HWT participants viewed initiating convection in the central United States from GLM16 and GLM17 (Thiel 2022), and similar anomalies in GLM16 and GLM17 FED and TOE values to the two presented case studies were observed in regions of increased deep-layer shear. The displaced convective anvils to the east also provided GLM17 a more direct perspective of the storm's updrafts. Thiel (2022) also reported that from these observations, testbed participants supported increased dual-GLM training along with merged-GLM products in regions of overlap. Additionally, the day/night variations in GLM flash DE (Bateman et al. 2021) from each sensor may limit the optical energy differences to daytime convection, as both supercells occurred during the day.

6. Summary and conclusions

Gridded GLM products were examined with ABI clean-IR imagery, MRMS vertically integrated reflectivity products,

and one ground-based lightning network, to validate GLM imagery and provide applications when merged with other operational products. Two case studies of semidiscrete supercells in southeast Kansas (24 May 2019) and central Alabama (25 March 2021) provided storm scale observations and trends relative to convective evolution. A bulk, 7-week study of convection across the central and eastern United States then gave additional context and applications. Overall, the GLM gridded products provided complementary information with respect to convective evolution and severity potential. Similar to previous studies, the inverse relationship between local flash rate and area was identified using flash extent density and minimum flash area. Increasing FED coincided with decreasing MFA with respect to decreasing IR brightness temperatures and increasing isothermal reflectivity at $-10°C$, vertically integrated ice, and maximum expected size of hail within the bulk study. This relationship was especially apparent when isothermal reflectivity values exceeded 30 dBZ or when examining imagery near local storm reports. During both case studies, increasing FED and decreasing MFA coincided temporally with increasing intensity from the MRMS variables and the convective evolution of each storm, and during the 24 May 2019 Kansas supercell even preceded the development of a robust mesocyclone. This FED–MFA signal, when combined with other radar and satellite observations, may provide additional confidence that a thunderstorm is intensifying, and therefore, its potential to produce severe weather is increasing. When examining the differences in viewing angles from GOES-East and GOES-West of the same storm, MFA provided more consistent signals near the edge of the field of view making it a useful product for evaluating updraft intensity when paired with FED. Additionally, larger MFA values were discovered between clean-IR brightness temperatures of 210–230 K and $-10°C$ isothermal reflectivity values from 20 to 30 dBZ, which can help forecasters identify regions where larger flashes are more likely such as in stratiform precipitation.

Throughout the study, GLM total optical energy values displayed multiple dependencies, which were especially apparent with GLM-to-GLM intercomparisons within the two supercell case studies. In both case studies, the western perspective of the *GOES-17* GLM provided a more direct observation of flashes within the updraft, which during periods of intensification led to rapid increases in TOE observations from the *GOES-17* GLM but not the *GOES-16* GLM. While previous studies suggest that the GOES-East GLM provides improved detection efficiencies for areas east of 103°W, and vice versa for the GOES-West GLM, operationally useful information regarding the quality of GLM observations may be available when using GLM data from both perspectives. Variability in local and storm-total flash rates from each GLM further supported these results, as peaks in the *GOES-17* TOE corresponded with times of comparable FED and storm-total flash rates when compared to the *GOES-16* GLM. These results suggest greater exploration of the total optical energy product from the GOES-East and GOES-West GLM perspectives is needed to fully assess GLM data quality, and that dual-GLM observations of severe convective storms in regions of sensor overlap may provide critical context to the flash characteristics observed from each GLM with respect to other observing platforms such as satellite imagery and radar. In an operational environment, limited screen space and task saturation by forecasters in convective scenarios may inhibit the use of dual-GLM observations. Therefore, automated data fusion methods that leverage machine learning such as ProbSevere (Cintineo et al. 2020) may be able to simplify this task when monitoring convection while still providing operational forecasters critical information with respect to thunderstorm evolution.

Data availability statement. GOES-R series GLM and ABI data can be found through NOAA CLASS (https://www.class.noaa.gov/), Google Cloud (https://console.cloud.google.com/marketplace/partners/noaa-public), and Amazon Web Services (https://registry.opendata.aws/noaa-goes/). GLM gridded imagery were created using the glmtools (Bruning 2019) software package. *Storm Data* events were accessed from the NCEI Storm Events Database (https://www.ncdc.noaa.gov/stormevents/). Cartopy (Elson et al. 2018), Matplotlib (Hunter 2007), MetPy (May et al. 2022), and Seaborn (Waskom et al. 2020) were used to create all figures.

REFERENCES

Adler, R. F., M. J. Markus, D. D. Fenn, G. Szejwach, and W. E. Shenk, 1983: Thunderstorm top structure observed by aircraft overflights with an infrared radiometer. *J. Climate Appl. Meteor.*, **22**, 579–593, https://doi.org/10.1175/1520-0450(1983)022<0579:TTSOBA>2.0.CO;2.

——, ——, and ——, 1985: Detection of severe Midwest thunderstorms using geosynchronous satellite data. *Mon. Wea. Rev.*, **113**, 769–781, https://doi.org/10.1175/1520-0493(1985)113<0769:DOSMTU>2.0.CO;2.

Bateman, M., D. Mach, and M. Stock, 2021: Further investigation into detection efficiency and false alarm rate for the geostationary lightning mappers aboard GOES-16 and GOES-17. *Earth Space Sci.*, **8**, e2020EA001237, https://doi.org/10.1029/2020EA001237.

Bedka, K., J. Brunner, R. Dworak, W. Feltz, J. Otkin, and T. Greenwald, 2010: Objective satellite-based detection of overshooting tops using infrared window channel brightness temperature gradients. *J. Appl. Meteor. Climatol.*, **49**, 181–202, https://doi.org/10.1175/2009JAMC2286.1.

——, E. M. Murillo, C. R. Homeyer, B. Scarino, and H. Mersiovsky, 2018: The above-anvil cirrus plume: An important severe weather indicator in visible and infrared satellite imagery. *Wea. Forecasting*, **33**, 1159–1181, https://doi.org/10.1175/WAF-D-18-0040.1.

Bruning, E. C., 2019: deeplycloudy/glmtools: glmtools release to accompany publication. Zenodo, accessed 5 March 2020, https://doi.org/10.5281/zenodo.2648658.

——, and D. R. MacGorman, 2013: Theory and observations of controls on lightning flash size spectra. *J. Atmos. Sci.*, **70**, 4012–4029, https://doi.org/10.1175/JAS-D-12-0289.1.

——, and Coauthors, 2019: Meteorological imagery for the geostationary lightning mapper. *J. Geophys. Res. Atmos.*, **124**, 14 285–14 309, https://doi.org/10.1029/2019JD030874.

Brunner, K. N., and P. M. Bitzer, 2020: A first look at cloud inhomogeneity and its effect on lightning optical emission. *Geophys. Res. Lett.*, **47**, e2020GL087094, https://doi.org/10.1029/2020GL087094.

Buechler, D. E., and S. J. Goodman, 1990: Echo size and asymmetry: Impact on NEXRAD storm identification. *J. Appl. Meteor.*, **29**, 962–969, https://doi.org/10.1175/1520-0450(1990)029<0962:ESAAIO>2.0.CO;2.

Bunkers, M. J., B. A. Klimowski, J. W. Zeitler, R. L. Thompson, and M. L. Weisman, 2000: Predicting supercell motion using a new hodograph technique. *Wea. Forecasting*, **15**, 61–79, https://doi.org/10.1175/1520-0434(2000)015<0061:PSMUAN>2.0.CO;2.

Calhoun, K. M., 2018: Feedback and recommendations for the Geostationary Lightning Mapper (GLM) in severe and hazardous weather forecasting and warning operations. GOES Proving Ground Tech. Rep., 15 pp., https://hwt.nssl.noaa.gov/ewp/projects/GLM-HWT-report_2018.pdf.

——, 2019: Feedback and recommendations for the Geostationary Lightning Mapper (GLM) in severe and hazardous weather forecasting and warning operations. GOES Proving Ground Tech. Rep., 16 pp., https://hwt.nssl.noaa.gov/ewp/projects/GLM-HWT-report-2019.pdf.

——, D. R. MacGorman, C. L. Ziegler, and M. I. Biggerstaff, 2013: Evolution of lightning activity and storm charge relative to dual-Doppler analysis of a high-precipitation supercell storm. *Mon. Wea. Rev.*, **141**, 2199–2223, https://doi.org/10.1175/MWR-D-12-00258.1.

——, E. R. Mansell, D. R. MacGorman, and D. C. Dowell, 2014: Numerical simulations of lightning and storm charge of the 29–30 May 2004 Geary, Oklahoma, supercell thunderstorm using EnKF mobile radar data assimilation. *Mon. Wea. Rev.*, **142**, 3977–3997, https://doi.org/10.1175/MWR-D-13-00403.1.

——, E. C. Bruning, and C. J. Schultz, 2018: Principles and operational applications of geostationary lightning mapper data for severe local storms. *29th Conf. on Severe Local Storms*, Stowe, VT, Amer. Meteor. Soc., 2.3, https://ams.confex.com/ams/29SLS/webprogram/Paper348316.html.

——, K. L. Berry, D. M. Kingfield, T. Meyer, M. J. Krocak, T. M. Smith, G. Stumpf, and A. Gerard, 2021: The experimental warning program of NOAA's Hazardous Weather Testbed. *Bull. Amer. Meteor. Soc.*, **102**, E2229–E2246, https://doi.org/10.1175/BAMS-D-21-0017.1.

Carey, L. D., and S. A. Rutledge, 2000: The relationship between precipitation and lightning in tropical island convection: A C-band polarimetric radar study. *Mon. Wea. Rev.*, **128**, 2687–2710, https://doi.org/10.1175/1520-0493(2000)128<2687:TRBPAL>2.0.CO;2.

——, E. V. Schultz, C. J. Schultz, W. Deierling, W. A. Petersen, A. L. Bain, and K. E. Pickering, 2019: An evaluation of relationships between radar-inferred kinematic and microphysical parameters and lightning flash rates in Alabama storms. *Atmosphere*, **10**, 796, https://doi.org/10.3390/atmos10120796.

Cintineo, J. L., M. J. Pavolonis, J. M. Sieglaff, L. Cronce, and J. Brunner, 2020: NOAA ProbSevere v2.0? ProbHail, ProbWind, and ProbTor. *Wea. Forecasting*, **35**, 1523–1543, https://doi.org/10.1175/WAF-D-19-0242.1.

Cummins, K. L., and M. J. Murphy, 2009: An overview of lightning locating systems: History, techniques, and data uses, with an in-depth look at the U.S. NLDN. *IEEE Trans. Electromagn. Compat.*, **51**, 499–518, https://doi.org/10.1109/TEMC.2009.2023450.

Elsenheimer, C. B., and C. M. Gravelle, 2019: Introducing lightning threat messaging using the *GOES-16* day cloud phase distinction RGB composite. *Wea. Forecasting*, **34**, 1587–1600, https://doi.org/10.1175/WAF-D-19-0049.1.

Elson, P., and Coauthors, 2018: SciTools/cartopy: v0.17.0. Zenodo, accessed 11 April 2020, https://doi.org/10.5281/zenodo.1490296.

Emersic, C., and C. Saunders, 2010: Further laboratory investigations into the relative diffusional growth rate theory of thunderstorm electrification. *Atmos. Res.*, **98**, 327–340, https://doi.org/10.1016/j.atmosres.2010.07.011.

Flournoy, M. D., M. C. Coniglio, and E. N. Rasmussen, 2021: Examining relationships between environmental conditions and supercell motion in time. *Wea. Forecasting*, **36**, 737–755, https://doi.org/10.1175/WAF-D-20-0192.1.

Goodman, S. J., D. Mach, W. Koshak, and R. Blakeslee, 2012: GLM lightning cluster-filter algorithm. NOAA/NESDIS, 73 pp., https://www.star.nesdis.noaa.gov/goesr/documents/ATBDs/Baseline/ATBD_GOES-R_GLM_v3.0_Jul2012.pdf.

——, and Coauthors, 2013: The GOES-R Geostationary Lightning Mapper (GLM). *Atmos. Res.*, **125–126**, 34–49, https://doi.org/10.1016/j.atmosres.2013.01.006.

Greene, D. R., and R. A. Clark, 1972: Vertically integrated liquid water—A new analysis tool. *Mon. Wea. Rev.*, **100**, 548–552, https://doi.org/10.1175/1520-0493(1972)100<0548:VILWNA>2.3.CO;2.

Heidinger, A., 2013: Algorithm theoretical basis document: ABI cloud height. NOAA/NESDIS, 79 pp., https://www.star.nesdis.noaa.gov/goesr/docs/ATBD/Cloud_Height.pdf.

——, and W. Straka, 2013: Algorithm theoretical basis document: ABI cloud mask. NOAA/NESDIS, 106 pp., https://www.star.nesdis.noaa.gov/goesr/docs/ATBD/Cloud_Mask.pdf.

Hondl, K. D., and M. D. Eilts, 1994: Doppler radar signatures of developing thunderstorms and their potential to indicate the onset of cloud-to-ground lightning. *Mon. Wea. Rev.*, **122**, 1818–1836, https://doi.org/10.1175/1520-0493(1994)122<1818:DRSODT>2.0.CO;2.

Hunter, J. D., 2007: Matplotlib: A 2D graphics environment. *Comput. Sci. Eng.*, **9**, 90–95, https://doi.org/10.1109/MCSE.2007.55.

Kelly, D. L., J. T. Schaefer, and C. A. Doswell, 1985: Climatology of nontornadic severe thunderstorm events in the United States. *Mon. Wea. Rev.*, **113**, 1997–2014, https://doi.org/10.1175/1520-0493(1985)113<1997:CONSTE>2.0.CO;2.

Kuhlman, K. M., D. R. MacGorman, M. I. Biggerstaff, and P. R. Krehbiel, 2009: Lightning initiation in the anvils of two supercell storms. *Geophys. Res. Lett.*, **36**, L07802, https://doi.org/10.1029/2008GL036650.

Lakshmanan, V., T. Smith, K. Hondl, G. J. Stumpf, and A. Witt, 2006: A real-time, three-dimensional, rapidly updating, heterogeneous radar merger technique for reflectivity, velocity, and derived products. *Wea. Forecasting*, **21**, 802–823, https://doi.org/10.1175/WAF942.1.

Light, T. E., D. M. Suszcynsky, M. W. Kirkland, and A. R. Jacobson, 2001: Simulations of lightning optical waveforms as seen through

clouds by satellites. *J. Geophys. Res.*, **106**, 17 103–17 114, https://doi.org/10.1029/2001JD900051.

MacGorman, D. R., A. A. Few, and T. L. Teer, 1981: Layered lightning activity. *J. Geophys. Res.*, **86**, 9900, https://doi.org/10.1029/JC086iC10p09900.

Mahalik, M. C., B. R. Smith, K. L. Elmore, D. M. Kingfield, K. L. Ortega, and T. M. Smith, 2019: Estimates of gradients in radar moments using a linear least squares derivative technique. *Wea. Forecasting*, **34**, 415–434, https://doi.org/10.1175/WAF-D-18-0095.1.

Makowski, J. A., D. R. MacGorman, M. I. Biggerstaff, and W. H. Beasley, 2013: Total lightning characteristics relative to radar and satellite observations of Oklahoma mesoscale convective systems. *Mon. Wea. Rev.*, **141**, 1593–1611, https://doi.org/10.1175/MWR-D-11-00268.1.

Maneewongvatana, S., and D. M. Mount, 1999: Analysis of approximate nearest neighbor searching with clustered point sets. arXiv, 9901013v1, https://doi.org/10.48550/arXiv.cs/9901013.

May, R. M., and Coauthors, 2022: MetPy: A meteorological Python library for data analysis and visualization. *Bull. Amer. Meteor. Soc.*, **103**, E2273–E2284, https://doi.org/10.1175/BAMS-D-21-0125.1.

Mecikalski, R. M., and L. D. Carey, 2018: Radar reflectivity and altitude distributions of lightning flashes as a function of three main storm types. *J. Geophys. Res. Atmos.*, **123**, 12 814–12 828, https://doi.org/10.1029/2018JD029238.

Mosier, R. M., C. Schumacher, R. E. Orville, and L. D. Carey, 2011: Radar nowcasting of cloud-to-ground lightning over Houston, Texas. *Wea. Forecasting*, **26**, 199–212, https://doi.org/10.1175/2010WAF2222431.1.

Murphy, M. J., and R. K. Said, 2020: Comparisons of lightning rates and properties from the U.S. National Lightning Detection Network (NLDN) and GLD360 with GOES-16 Geostationary Lightning Mapper and advanced baseline imager data. *J. Geophys. Res. Atmos.*, **125**, e2019JD031172, https://doi.org/10.1029/2019JD031172.

Petersen, D., and W. H. Beasley, 2013: High-speed video observations of a natural negative stepped leader and subsequent dart-stepped leader. *J. Geophys. Res. Atmos.*, **118**, 12 110–12 119, https://doi.org/10.1002/2013JD019910.

Peterson, M., 2019: Research applications for the Geostationary Lightning Mapper operational lightning flash data product. *J. Geophys. Res. Atmos.*, **124**, 10 205–10 231, https://doi.org/10.1029/2019JD031054.

——, 2020: Modeling the transmission of optical lightning signals through complex 3-D cloud scenes. *J. Geophys. Res. Atmos.*, **125**, e2020JD033231, https://doi.org/10.1029/2020JD033231.

——, 2021: Holes in optical lightning flashes: Identifying poorly transmissive clouds in lightning imager data. *Earth Space Sci.*, **8**, e2020EA001294, https://doi.org/10.1029/2020EA001294.

——, S. Rudlosky, and D. Zhang, 2020: Changes to the appearance of optical lightning flashes observed from space according to thunderstorm organization and structure. *J. Geophys. Res. Atmos.*, **125**, e2019JD031087, https://doi.org/10.1029/2019JD031087.

Potvin, C. K., C. Broyles, P. S. Skinner, H. E. Brooks, and E. Rasmussen, 2019: A Bayesian hierarchical modeling framework for correcting reporting bias in the U.S. tornado database. *Wea. Forecasting*, **34**, 15–30, https://doi.org/10.1175/WAF-D-18-0137.1.

Reynolds, D. W., 1980: Observations of damaging hailstorms from geosynchronous satellite digital data. *Mon. Wea. Rev.*, **108**, 337–348, https://doi.org/https://doi.org/10.1175/1520-0493(1980)108<0337:OODHFG>2.0.CO;2.

Rison, W., R. J. Thomas, P. R. Krehbiel, T. Hamlin, and J. Harlin, 1999: A GPS-based three-dimensional lightning mapping system: Initial observations in central New Mexico. *Geophys. Res. Lett.*, **26**, 3573–3576, https://doi.org/10.1029/1999GL010856.

Roberts, R. D., and S. Rutledge, 2003: Nowcasting storm initiation and growth using *GOES-8* and WSR-88D data. *Wea. Forecasting*, **18**, 562–584, https://doi.org/10.1175/1520-0434(2003)018<0562:NSIAGU>2.0.CO;2.

Rotunno, R., and J. B. Klemp, 1982: The influence of the shear-induced pressure gradient on thunderstorm motion. *Mon. Wea. Rev.*, **110**, 136–151, https://doi.org/10.1175/1520-0493(1982)110<0136:TIOTSI>2.0.CO;2.

Rudlosky, S. D., 2015: Evaluating ENTLN performance relative to TRMM/LIS. *J. Oper. Meteor.*, **3**, 11–20, https://doi.org/10.15191/nwajom.2015.0302.

——, and K. S. Virts, 2021: Dual Geostationary Lightning Mapper observations. *Mon. Wea. Rev.*, **149**, 979–998, https://doi.org/10.1175/MWR-D-20-0242.1.

——, S. J. Goodman, K. S. Virts, and E. C. Bruning, 2019: Initial Geostationary Lightning Mapper observations. *Geophys. Res. Lett.*, **46**, 1097–1104, https://doi.org/10.1029/2018GL081052.

Rutledge, S. A., K. A. Hilburn, A. Clayton, B. Fuchs, and S. D. Miller, 2020: Evaluating Geostationary Lightning Mapper flash rates within intense convective storms. *J. Geophys. Res. Atmos.*, **125**, e2020JD032827, https://doi.org/10.1029/2020JD032827.

Sandmæl, T. N., B. R. Smith, J. G. Madden, J. W. Monroe, P. T. Hyland, B. A. Schenkel, and T. C. Meyer, 2023: The 2021 Hazardous Weather Testbed Experimental Warning Program radar convective applications experiment: A forecaster evaluation of the tornado probability algorithm and the new mesocyclone detection algorithm. *Wea. Forecasting*, **38**, 1125–1142, https://doi.org/10.1175/WAF-D-23-0042.1.

Schmit, T. J., M. Gunshor, G. Fu, T. Rink, K. Bah, W. Zhang, and W. Wolf, 2012: GOES-R Advanced Baseline Imager (ABI) algorithm theoretical basis document for Cloud And Moisture Imagery Product (CMIP). NOAA/NESDIS, 63 pp., https://www.star.nesdis.noaa.gov/goesr/docs/ATBD/Imagery.pdf.

——, P. Griffith, M. M. Gunshor, J. M. Daniels, S. J. Goodman, and W. J. Lebair, 2017: A closer look at the ABI on the GOES-R series. *Bull. Amer. Meteor. Soc.*, **98**, 681–698, https://doi.org/10.1175/BAMS-D-15-00230.1.

Schultz, C. J., W. A. Petersen, and L. D. Carey, 2009: Preliminary development and evaluation of lightning jump algorithms for the real-time detection of severe weather. *J. Appl. Meteor. Climatol.*, **48**, 2543–2563, https://doi.org/10.1175/2009JAMC2237.1.

——, L. D. Carey, E. V. Schultz, and R. J. Blakeslee, 2015: Insight into the kinematic and microphysical processes that control lightning jumps. *Wea. Forecasting*, **30**, 1591–1621, https://doi.org/10.1175/WAF-D-14-00147.1.

——, ——, ——, and ——, 2017: Kinematic and microphysical significance of lightning jumps versus nonjump increases in total flash rate. *Wea. Forecasting*, **32**, 275–288, https://doi.org/10.1175/WAF-D-15-0175.1.

Smith, T. M., and Coauthors, 2016: Multi-Radar Multi-Sensor (MRMS) severe weather and aviation products: Initial operating capabilities. *Bull. Amer. Meteor. Soc.*, **97**, 1617–1630, https://doi.org/10.1175/BAMS-D-14-00173.1.

Stolzenburg, M., T. C. Marshall, and P. R. Krehbiel, 2015: Initial electrification to the first lightning flash in New Mexico thunderstorms. *J. Geophys. Res. Atmos.*, **120**, 11253–11276, https://doi.org/10.1002/2015JD023988.

Stough, S. M., L. D. Carey, C. J. Schultz, and P. M. Bitzer, 2017: Investigating the relationship between lightning and mesocyclonic rotation in supercell thunderstorms. *Wea. Forecasting*, **32**, 2237–2259, https://doi.org/10.1175/WAF-D-17-0025.1.

Strassberg, G., and M. Sowko, 2021: National Weather Service instruction 10-1605: Performance and evaluation, NWSPD 10-16 storm data preparation. NOAA NCEI Tech. Rep., 110 pp., https://www.nws.noaa.gov/directives/sym/pd01016005curr.pdf.

Takahashi, T., 1978: Riming electrification as a charge generation mechanism in thunderstorms. *J. Atmos. Sci.*, **35**, 1536–1548, https://doi.org/10.1175/1520-0469(1978)035<1536:REAACG>2.0.CO;2.

Thiel, K., 2022: GOES-R and JPSS proving ground demonstration at the Hazardous Weather Testbed 2022 Spring Experiment final evaluation. Cooperative Institute for Severe and High-Impact Weather Research and Operations Tech. Rep. 47 pp., https://doi.org/10.25923/fwnq-kf73.

——, and K. Calhoun, 2021: GOES-R and JPSS proving ground demonstration at the Hazardous Weather Testbed 2021 Spring Experiment final evaluation. Cooperative Institute for Severe and High-Impact Weather Research and Operations Tech. Rep., 35 pp., https://doi.org/10.25923/ksf3-js29.

——, K. M. Calhoun, A. E. Reinhart, and D. R. MacGorman, 2020: GLM and ABI characteristics of severe and convective storms. *J. Geophys. Res. Atmos.*, **125**, e2020JD032858, https://doi.org/10.1029/2020JD032858.

Thomas, R. J., P. R. Krehbiel, W. Rison, T. Hamlin, D. J. Boccippio, S. J. Goodman, and H. J. Christian, 2000: Comparison of ground-based 3-dimensional lightning mapping observations with satellite-based LIS observations in Oklahoma. *Geophys. Res. Lett.*, **27**, 1703–1706, https://doi.org/10.1029/1999GL010845.

Thomson, L. W., and E. P. Krider, 1982: The effects of clouds on the light produced by lightning. *J. Atmos. Sci.*, **39**, 2051–2065, https://doi.org/10.1175/1520-0469(1982)039<2051:TEOCOT>2.0.CO;2.

Trapp, R. J., D. M. Wheatley, N. T. Atkins, R. W. Przybylinski, and R. Wolf, 2006: Buyer beware: Some words of caution on the use of severe wind reports in postevent assessment and research. *Wea. Forecasting*, **21**, 408–415, https://doi.org/10.1175/WAF925.1.

Waskom, M., and Coauthors, 2020: mwaskom/seaborn: v0.10.0 (January 2020). Zenodo, accessed 11 April 2020, https://doi.org/10.5281/zenodo.3629446.

Weiss, S. A., D. R. MacGorman, and K. M. Calhoun, 2012: Lightning in the anvils of supercell thunderstorms. *Mon. Wea. Rev.*, **140**, 2064–2079, https://doi.org/10.1175/MWR-D-11-00312.1.

Williams, E. R., 1985: Large-scale charge separation in thunderclouds. *J. Geophys. Res.*, **90**, 6013, https://doi.org/10.1029/JD090iD04p06013.

——, and Coauthors, 1999: The behavior of total lightning activity in severe Florida thunderstorms. *Atmos. Res.*, **51**, 245–265, https://doi.org/10.1016/S0169-8095(99)00011-3.

Witt, A., M. D. Eilts, G. J. Stumpf, J. T. Johnson, E. D. Mitchell, and K. W. Thomas, 1998: An enhanced hail detection algorithm for the WSR-88D. *Wea. Forecasting*, **13**, 286–303, https://doi.org/10.1175/1520-0434(1998)013<0286:AEHDAF>2.0.CO;2.

Wolf, P., 2006: Anticipating the initiation, cessation, and frequency of cloud-to-ground lightning, utilizing WSR-88D reflectivity data. *NWA Electronic J. Oper. Meteor.*, 19 pp., http://nwafiles.nwas.org/ej/pdf/2007-EJ1.pdf.

Woodard, C. J., L. D. Carey, W. A. Petersen, and W. P. Roeder, 2012: Operational utility of dual-polarization variables in lightning initiation forecasting. *Electron. J. Oper. Meteor.*, **13**, 79–102.

Zhang, D., and K. L. Cummins, 2020: Time evolution of satellite-based optical properties in lightning flashes, and its impact on GLM flash detection. *J. Geophys. Res. Atmos.*, **125**, e2019JD032024, https://doi.org/10.1029/2019JD032024.

Zhu, Y., and Coauthors, 2017: Evaluation of ENTLN performance characteristics based on the ground truth natural and rocket-triggered lightning data acquired in Florida: Evaluation of ENTLN performance. *J. Geophys. Res. Atmos.*, **122**, 9858–9866, https://doi.org/10.1002/2017JD027270.

——, M. Stock, J. Lapierre, and E. DiGangi, 2022: Upgrades of the Earth networks total lightning network in 2021. *Remote Sens.*, **14**, 2209, https://doi.org/10.3390/rs14092209.